Lattice dynamics of ultrathin layers of KBr grown epitaxially on RbCl(001)

E. S. Gillman,* Jeff Baker, J. J. Hernandez, G. G. Bishop, J. A. Li, S. A. Safron, and J. G. Skofronick
Departments of Physics and Chemistry and Center for Materials Research and Technology, Florida State University, Tallahassee, Florida 32306

D. Bonart and U. Schröder
Institut für Theoretische Physik, Universität Regensburg, Universitätsstrasse 32, 93040 Regensburg, Germany
(Received 4 August 1995; revised manuscript received 8 December 1995)

High-resolution helium-atom scattering experiments were performed on epitaxially grown layers of KBr on a RbCl(001) substrate for films 1, 2, and 3 ML thick. The layer-by-layer growth was monitored *in situ* by measuring the intensity of the specularly scattered He beam versus coverage. Measurements of the single-phonon inelastic scattering were carried out on each succeeding layer to determine the surface-phonon dispersion in both the $\overline{\Gamma M}$ and $\overline{\Gamma X}$ high-symmetry directions of the surface Brillouin zone. Shell-model potential parameters were determined in a consistent fashion for the four anion-cation constituents at the interface, which gave a good fit to the dispersion curve data from 1-, 2-, and 3-ML KBr/RbCl epitaxially grown systems as reported in this study and, in addition, the bulk and clean surface dispersions of KBr, RbCl, KCl, and RbBr were fit by the same parameters.

I. INTRODUCTION

Studies of epitaxial growth have a long history to which many experimental approaches have contributed.[1,2] In molecular-beam epitaxy (MBE) the most generally used method for following the growth and determining the crystalline quality is reflection high-energy electron diffraction (RHEED).[2,3] This technique is employed due to the relative ease of displaying the real-time oscillatory behavior of the diffraction peak intensities as layer-by-layer growth occurs. In addition, RHEED patterns can provide information about the size of the growing islands and the step height if the scattering of the electron beam from the islands and the substrate is measured as a function of the incident beam energy or angle.

A major shortcoming of RHEED is that it cannot easily supply information about the vibrational dynamics. This limitation is unfortunate, since it is the surface and interfacial dynamics that largely determine the growth mechanism. Furthermore, when RHEED is used on insulating surfaces radiation damage and surface charging can occur during the monitoring.[4–6] In recent years it has become clear that the simple kinematic analysis of the RHEED data is not always sufficient to explain some of the unusual RHEED measurements made during growth. This problem arises mainly because electron scattering requires a treatment that takes into account multiple scattering collisions as well as penetration into the bulk,[2,7]

In recent studies structural data and layer-by-layer monitoring of the growth process have also been forthcoming using neutral helium-atom scattering (HAS).[8–13] Although not as widely used as RHEED, HAS has two distinct advantages. These are (1) the He atoms do not penetrate the surface and (2) scattering conditions can be realized where single-phonon collisions dominate. Thus, while similar intensity oscillations and interference effects are measured, simple kinematic arguments are often justified with HAS. Furthermore, as HAS employs low-energy neutral particles, damage from inelastic collisions and charging effects on insulator surfaces are never a problem. More significantly, HAS offers the opportunity for surface dynamical studies of epitaxially deposited films, as was shown in the pioneering work of Gibson and Sibener for physisorbed layers of rare gases on Ag(111).[12,13] Since that report, there has been a steady output of results from HAS investigations of both surface structure and dynamics of epitaxial surfaces. A summary of HAS growth studies that include dynamical results is given in Table I.

The alkali halides, as the archetypical ionic insulators, provide the opportunity to examine the relationship between dynamics and growth under easily controlled experimental conditions. The lattice spacing, ionic radii, and range of masses all lend themselves to studies over a wide range of conditions. Further, the dynamics of these pure materials, including both bulk and surface phonon dispersion, have been thoroughly examined and interpreted *via* the shell model.[14,15] Some initial work on the growth of the alkali halides was done by Flynn and co-workers.[4,5] Using RHEED to monitor the epitaxial growth, they reported structural features of the adlayers, but did not measure any dynamics of the surface.

The first report on the use of HAS to study alkali halide growth was for the homoepitaxial system NaCl/NaCl(001).[16] Structure, island size, and layer thickness were determined. This was closely followed by a study of the heteroepitaxial growth for the KBr/NaCl system, which has a large lattice mismatch (17%) and preliminary work for the KBr/RbCl(001) system, which has a very small mismatch (0.12%).[17,18] In both cases, the materials have face-centered cubic (fcc) lattices with the rocksalt structure. In the work reported here, the KBr/RbCl system is studied in much greater detail than in the previous work.

Both KBr and RbCl can be well described using the shell model, allowing for a theoretical analysis of the layered sys-

TABLE I. Thin-film phonon studies.

System	No. of layers	Reference
Ar,Kr,Xe/Ag(111)	1,2,3,25	Gibson[a]
Ar/Pt(111)	1,2,3	Gibson[a]
Ar,Kr,Xe/Ag(111)	1,2,3	Gibson[b]
Kr/Pt(111)	1,2,3	Hall[c]
KBr/NaCl(001)	2,3,4,7	Safron[d]
NaCl/Ge(001)	1,2,3,10	Brusdeylins[e]
KBr/RbCl(001)	1	Safron[f]
Ag/Ni(001)	1,2,3,50	Daum[g]
Fe/Cu(001)	1,2,3,5	Daum[h]
NaCl/NaCl(001)	1,5	Duan[i]
Ag/Cu(100)	1	Duam[i]
Co/Cu(001)	1,2,3,16	Mohamed[j]
Ni/Cu(001)	2,3,4,6	Mohamed[k]
Ni/Cu(001)	2,4	Chen[l]
Pb/Cu(111)	0.5,1,3–10,30	Hinch[m]
Na/Cu(001)	1–15,30	Benedek[n]
Pb/Ge(111)	3,4,5,6,20	Schmidt[o]
Pb/Si(111)	2,3,4,12	Schmicker[p]
KBr/RbCl(001)	1	Skofronick[q]
KBr/RbCl(001)	1	Bonart[r]

[a]K. D. Gibson and S. J. Sibener, Phys. Rev. Lett. **55**, 514 (1985); Farad. Discuss. Chem. Soc. **80**, 203 (1985).
[b]K. D. Gibson and S. J. Sibener, J. Chem. Phys. **88**, 7862 (1988).
[c]B. Hall, D. L. Mills, P. Zeppenfeld, K. Kern, U. Becker, and G. Comsa, Phys. Rev. B **40**, 6326 (1989).
[d]S. A. Safron, G. G. Bishop, J. Duan, E. S. Gillman, J. G. Skofronick, N. S. Luo, and P. Ruggerone, J. Phys. Chem. **97**, 2270 (1992).
[e]G. Brusdeylins, N. S. Luo, P. Ruggerone, D. Schmicker, J. P. Toennies, R. Vollmer, and Th. Wach, Surf. Sci. **272**, 358 (1992).
[f]S. A. Safron, J. Duan, G. G. Bishop, E. S. Gillman, and J. G. Skofronick, J. Phys. Chem. **97**, 1749 (1993).
[g]W. Daum, J. Electron. Spectrosc. Relat. Phenom. **44**, 271 (1987).
[h]W. Daum, C. Stuhlmann, and H. Ibach, Phys. Rev. Lett. **60**, 2741 (1988).
[i]J. Duan, G. G. Bishop, E. S. Gillman, G. Chern, S. A. Safron, and J. G. Skofronick, J. Vac. Sci. Technol. A **10**, 1999 (1992).
[j]M. H. Mohamed, J. S. Kim, and L. L. Kesmodel, Surf. Sci. **220**, L687 (1989).
[k]M. H. Mohamed, J. S. Kim, and L. L. Kesmodel, Phys. Rev. B **40**, 1305 (1989).
[l]Y. Chen, S. Y. Tang, J. S. Kim, M. H. Mohamed, and L. L. Kesmodel, Phys. Rev. B **43**, 6788 (1991).
[m]B. J. Hinch, C. Koziol, J. P. Toennies, and G. Zhang, Europhys. Lett. **10**, 341 (1989).
[n]G. Benedek, J. Ellis, A. Reichmuth, P. Ruggerone, H. Schief, and P. Toennies, Phys. Rev. Lett. **69**, 2951 (1992).
[o]S. Schmidt, Diplomarbeit Univ. of Göttingen, 1992.
[p]D. Schmicker, Doktorabeit Univ. of Göttingen, 1992.
[q]J. G. Skofronick, G. G. Bishop, J. Duan, E. S. Gillman, S. A. Safron, D. Bonart, and U. Schröder, J. Electron. Spectrosc. Relat. Phenom. **64/65**, 747 (1993).
[r]D. Bonart, Diplomarbeit, Univ. Regensburg (1993).

tem within this framework. Importantly, the computational effort is within reasonable limits as the lattice constants of the two alkali halide crystals are very nearly equal.[19–26] However, despite the similarities of the pairs of cations and anions, their sizes and polarizabilities are different, thus the shell-model parameters that work well for modeling the bulk and clean surface properties have had to be adapted to match the altered physical environment. As the shell model is the standard approach to the physics of ionic materials, its continued usefulness and evolution depends on its applicability.[14] Hence, an important result of this work is to establish the methodology for modifying the parameters in a consistent and physical way. A comparison with the calculations is presented here for the measured surface phonon dispersions in both high-symmetry directions for 1, 2, and 3 ML of KBr deposited onto the RbCl(001) substrate. Additionally, the bulk and surface dispersions curves for KBr, RbCl, KCl, and RbCl are also fit with the same common set of parameters.

In the next section we briefly describe the HAS instrument, including the apparatus used for the epitaxial growth studies. The experimental results are given in Sec. III. In Sec. IV, the shell-model analysis is presented; we discuss the results in Sec. V and give concluding remarks in Sec. VI.

II. EXPERIMENT

The apparatus employed for the experimental work is shown schematically in Fig. 1 and described briefly below. Details can be found in Ref. 9. Its design is similar to other HAS instruments described in the literature.[8,27,28] In this instrument, the helium beam is produced by a continuous expansion of helium gas from a nozzle located in the source chamber. The beam passes through a skimmer followed immediately by a chopper, which can be moved into or out of the beam path. After the beam passes the chopper stage, the helium atoms travel through two additional stages of differential pumping before entering into the scattering chamber where they collide with the target. The geometry of the system is fixed such that for the helium atoms to reach the detector the sum of their incident (θ_i) and final scattering angles (θ_f) must equal 90°. From the scattering chamber, the helium atoms travel through four stages of differential pumping before passing into the detector chamber where their flux is measured via an electric quadrupole mass spectrometer. Helium atoms not ionized in the electron bombardment ionizer pass through the quadrupole into a sump chamber where they are pumped away. The data acquisition system consists of a computer-controlled CAMAC crate that interfaces directly with the instrument. A manipulator holding the crystal target is used to align the surface of the crystal in the proper orientation by permitting translation in the x, y, and z directions, azimuthal rotation, and adjustment of the angle of tilt. It is mounted to the scattering chamber via a differentially pumped rotary seal so that the scattering angle may be adjusted without disturbing the alignment of the crystal.

With the chopper in the out-of-beam configuration, the total scattering intensity is measured vs incident angle (called an angular distribution). For ordered surfaces these measurements principally show the intensity of coherent elastic scattering from the surface (specular and Bragg diffraction) along with smaller selective adsorption features.[8,9] With the chopper in the in-beam chopper configuration, 7-μs pulses produced by the chopper are used in a time-of-

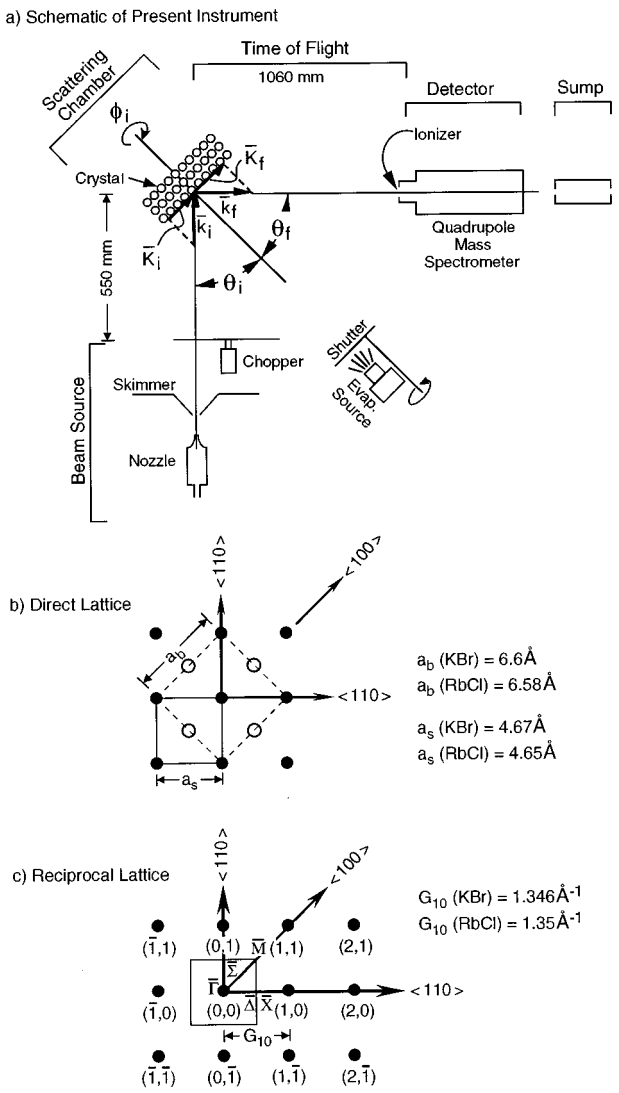

FIG. 1. (a) Schematic representation of the helium-atom scattering apparatus showing the beam source with nozzle and chopper, the scattering chamber containing both the evaporation source and the crystal target held by a manipulator (not shown), and the detector chamber with the quadrupole mass spectrometer. The source-detector angle is fixed at 90°. In (b) the direct and in (c) the reciprocal lattices for the fcc rocksalt (001) surface are shown. The dashed line in (b) is the projection of the bulk lattice and the solid line shows the surface unit cell. The square in (c) contains the first surface Brillouin zone and the area enclosed by $\bar{\Gamma}$ $\bar{x}$-$\bar{x}$ $\bar{M}$-$\bar{M}$ $\bar{\Gamma}$ is the irreducible element of the first Brillouin zone.

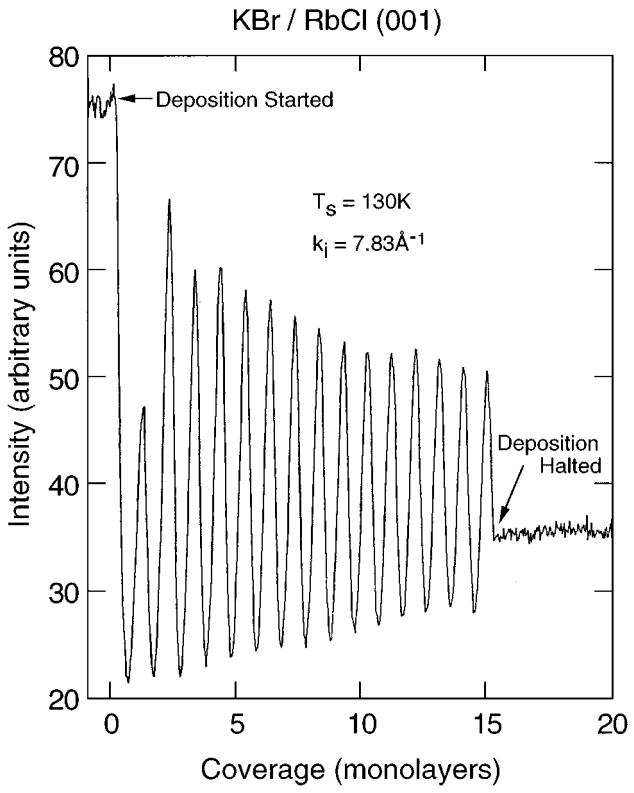

FIG. 2. Deposition curve for KBr onto the RbCl(001) substrate at a substrate temperature $T_s = 130$ K and incident He-atom wave vector $\mathbf{k}_i \approx 7.83$ Å^{-1}. The relative specular intensity is plotted as a function of coverage (monolayers). Each maxima (minima) corresponds to the completion of a monolayer (half-monolayer). The deposition could be routinely terminated at any point during the deposition. For the experiments reported here the deposition was stopped at one of the first three maxima corresponding to coverages of 1, 2, and 3 ML, respectively. The smaller amplitude of the first growth peak as compared to the rest is explained in the text.

flight (TOF) technique to provide an energy analysis of the intensity for any selected angle in the angular distribution.

The RbCl substrate used in this experiment was cleaved in air from a large boule obtained from the University of Utah Crystal Growth Laboratory to form a target that measured approximately 5mm×10 mm ×2 mm.[29] The target was quickly mounted on the manipulator and the scattering chamber then was evacuated and baked at ~200 °C for 24 h. An ultimate pressure of about 2×10^{-10} torr was achieved. The surface of the sample was routinely prepared prior to deposition by heating the sample to ~400°C for about 30–60 min, which was sufficient to sublime the topmost atomic layers and ensure a clean surface. After aligning the cleaved RbCl substrate in either the ⟨100⟩ or ⟨110⟩ direction, 1, 2, or 3 ML of KBr were deposited on the RbCl substrate. The coverage of the deposition was measured at the specular angle by monitoring the number of oscillations of the specular intensity with time (or coverage),[11,30–32] as shown in Fig. 2. Following the deposition, an angular distribution was performed to determine the structural changes that had taken place. This was followed with a series of TOF spectra to determine the lattice dynamics of the surface for each coverage. The majority of the measurements were made at target temperatures ~120–130 K. At higher temperatures the scattered signal was attenuated significantly by the Debye-Waller factor. At much lower temperatures the crystal became contaminated after a short time period, necessitating frequent cleaning. In Figs. 1(b) and 1(c) the rocksalt structure in real and reciprocal space are presented for these two fcc materials.

The deposition source, shown schematically in Fig. 1, consists of a single crystal of KBr (also obtained from the University of Utah Crystal Growth Laboratory), which was positioned ~14 cm from the RbCl target and resistively heated by a tungsten filament until the molecular flux from the sublimation of the KBr was sufficient for the desired growth rate.[29] The geometry of the deposition source was

such that the flux of KBr incident on the target was uniformly distributed. As a consequence, a beat pattern seen in the scattering intensity as a function of deposition time by Duan *et al.*[30] and attributed to nonuniformity of growth was not observed here. Although the temperature of the deposition source was not monitored, it was determined that the optimal conditions for layer-by-layer growth could be controlled by regulating the filament power supply at approximately 22 W. Depositions were routinely made under these conditions, which resulted in films of similar quality as was evidenced by their reproducible angular distributions. The time to deposit 1 ML was approximately 50–150 s.

III. EXPERIMENTAL RESULTS

Three types of experiments were performed with the HAS instrument: (1) depositions, which were monitored by measuring the specularly scattered helium-atom intensity vs coverage (deposition curves), (2) angular distributions of the scattered He atoms, and (3) TOF analysis of the scattered helium atoms. All of these measurements were done for coverages of 1, 2, and 3 ML in both high-symmetry directions of the KBr/RbCl(001) surface.

A. Deposition curves

The deposition curve shown in Fig. 2 is typical for two-dimensional layer-by-layer growth.[11,16,17,30,32] Before the deposition begins, the specular beam sees few defects or adsorbates and is at 75 arbitrary units on the ordinate scale of Fig. 2. For the *ideal* case of layer-by-layer growth, the intensity change of the specularly scattered He beam is primarily caused by two effects. The first and perhaps the most important effect is that during the initial growth, nucleation sites form, which grow into small islands. As the growth continues, the islands increase their size and eventually merge together, forming a 1-ML film. With continued deposition the process repeats, forming a 2-ML film, and so on. During the growth, island edges, defects, and disorder are present, which cause the beam to be scattered in directions other than the specular direction. Because of this loss of order, a decrease in the specularly scattered signal initially takes place as the KBr deposition is started. At about $\frac{1}{2}$-ML coverage, the nonspecular scattering reaches a maximum and the specular intensity falls to a minimum. As the deposited material increases beyond $\frac{1}{2}$ ML the spaces between the islands are filled in and the resulting specular intensity increases to a maximum as the surface order improves. This accounts for an oscillatory behavior that should ideally continue at the same amplitude with successive monolayers. In practice, defects and disorder effects accumulate to give a growth curve more like that in Fig. 2, where the minima are not so deep and the maxima gradually diminishes in intensity with increased number of deposited layers.

The second mechanism affecting the specularly scattered signal arises from constructive and destructive interference between the beam scattered from the substrate and the newly deposited epitaxial layer.[17,30] The phasing of the interference depends upon the transfer of momentum perpendicular to the surface, Δk_z, and can be selected for the desired phase condition.

What appears unusual in Fig. 2 is that the first maximum is much smaller than the succeeding ones. This was explained previously as being due to the different interference conditions for the larger spacing between the first KBr layer on RbCl as compared to subsequent layers of KBr on KBr.[17]

B. Angular distributions

Angular distribution experiments (described in Sec. II) are performed by measuring the total scattering intensity of the helium beam arriving at the detector as a function of incident angle of the beam. The periodic nature of the crystal surface imposes the criterion that the elastically scattered component of the incident helium beam obey the Bragg scattering relation for conservation of parallel momentum

$$\mathbf{K}_f - \mathbf{K}_i = \Delta\mathbf{K} = \mathbf{G}_{n,m}, \tag{1}$$

where $\mathbf{G}_{n,m}$ is a surface reciprocal lattice vector and $\mathbf{K}_i$ and $\mathbf{K}_f$ are the components of the incident and scattered wave vector parallel to the surface, respectively.[8–10] In terms of the incident and final wave vectors $\mathbf{k}_i$ and $\mathbf{k}_f$, and for the 90 ° configuration between the incident and scattered angles θ_i and θ_f, $\mathbf{K}_i = \mathbf{k}_i \sin\theta_i$ and $\mathbf{K}_f = \mathbf{k}_f \sin\theta_f$.

For the fcc crystals RbCl and KBr,

$$\mathbf{G}_{n,m} = \frac{2\pi n}{a_s}\hat{\mathbf{x}} + \frac{2\pi m}{a_s}\hat{\mathbf{y}}, \tag{2}$$

where $\hat{\mathbf{x}}$ and $\hat{\mathbf{y}}$ are the unit vectors for the surface reciprocal lattice, n and m are integers, and a_s is the surface lattice constant, which is related to the bulk lattice constant (a_b) by the relation $a_s = a_b/\sqrt{2}$. Figure 1(b) gives the bulk lattice dimensions. For the measurements reported here where the source-target-detector angle is fixed at 90°, as shown in Fig. 1(a), Eq. (1) can be written as

$$\Delta\mathbf{K} = \mathbf{G}_{m,n} = \mathbf{k}_i[\cos(\theta_i) - \sin(\theta_i)] = \sqrt{2}\mathbf{k}_i[\cos(\theta_i + \pi/4)]. \tag{3}$$

Figure 3 shows angular distributions for a coverage of 2 ML of KBr/RbCl(001) compared to the clean RbCl(001) substrate. What can be seen from these measurements is that for the clean RbCl(001) surface, the Bragg peaks in the $\langle 100\rangle$ direction are small compared to the specular peak and in the $\langle 100\rangle$ direction the Bragg peaks are considerably larger with the first-order Bragg peaks being comparable in magnitude to the specular peak. For the 2-ML case, this situation reverses itself: in the $\langle 100\rangle$ direction the first- and even the second-order Bragg peaks are comparable to the specular peak and for the $\langle 110\rangle$ direction the Bragg peaks are very small compared to the specular intensity. A significant fraction of this change is already observed for the 1-ML case and it continues to the 3-ML case (these angular distributions are not shown).

C. Time-of-flight measurements

TOF measurements (described in Sec. II) are used to determine the energy and momentum transfer between the surface and the scattering helium atoms. From Eq. (1) the coherent elastic peaks prominent in the angular distributions occur at scattering angles determined by the incident wave

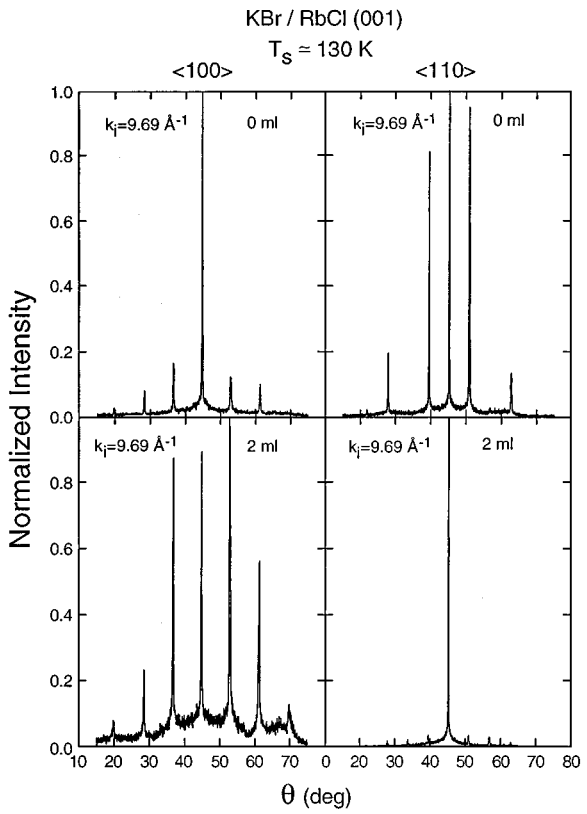

FIG. 3. Angular distributions of clean RbCl(001) and a 2-ML coverage of KBr/RbCl(001). The incident wave vector ($\mathbf{k}_i = 9.69$ Å^{-1}) and substrate temperature ($T_s = 130$ K) were the same for all four measurements.

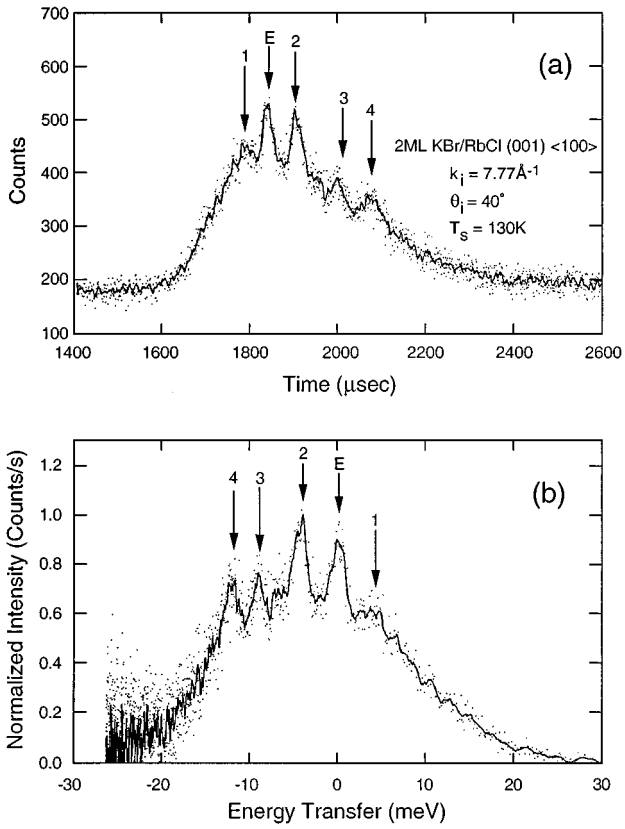

FIG. 4. Typical TOF distributions as a function of time (a) and converted into energy gains and losses (b) for KBr/RbCl(001) $\langle 100 \rangle$ ($k_i = 7.77$ Å^{-1}, $\theta_i = 40°$, $T_s = 130$ K, and $\Theta = 2$ ML). The peak labeled E is the diffuse elastic peak and the peaks labeled 1–4 are due to single-phonon creation-annihilation events. The base upon which the peaks are sitting is due to multiple phonon scattering. The data are shown as points and the solid line is a Savitzky-Golay smoothing of the data.

vector and the reciprocal lattice of the crystal target. Hence, any elastic scattering seen at other angles (termed incoherent or diffuse elastic scattering) must be due to defects or disorder on the surface. Thus, the TOF spectra also reveal the quality of the surface through the magnitude of the incoherent or diffuse elastic signal. Figure 4 shows a typical TOF distribution as a function of time (a) and converted to energy gains and losses (b) for KBr/RbCl(001) $\langle 100 \rangle$ ($k_i = 7.77$ Å^{-1}, $\theta_i = 40°$, $T_s = 130$ K, and $\Theta = 2$ ML). The peak labeled E is the diffuse elastic peak and the peaks labeled 1–4 are due to single-phonon creation-annihilation events. One should note that the peaks at negative energies correspond to creation of single phonons and, conversely, peaks at positive energies correspond to annihilation of single phonons.[8–10] The broad base or ''foot'' upon which the single-phonon peaks are sitting is due primarily to multiphonon scattering.[33] The relatively small diffuse elastic peak shown here, comparable to single-phonon peaks, is indicative of a relatively defect free film.

The TOF data from the single-phonon inelastic scattering events, when taken over a range of incident angles, map out the energy and momentum of the surface phonons across the surface Brillouin zone. The dispersion relations can be obtained through two simple kinematical relationships for single-phonon scattering: conservation of energy $\Delta E = \hbar\omega$, where $\hbar\omega$ is the energy of the phonon,

$$\Delta E = \frac{\hbar^2}{2m}(\mathbf{k}_f^2 - \mathbf{k}_i^2), \tag{4}$$

and conservation of momentum transfer parallel to the surface [an extension of Eq. (3)]

$$\Delta\mathbf{K} = \mathbf{K}_f - \mathbf{K}_i = \mathbf{Q} + \mathbf{G}_{n,m}, \tag{5}$$

where $\mathbf{Q}$ is the surface projection of the phonon wave vector and m is the mass of the helium atom. Combining Eqs. (4) and (5) and taking into account the scattering geometry [Fig. 1(a)] gives

$$\Delta E = \left[\frac{(\mathbf{k}_i \sin\theta_i + \Delta\mathbf{K})^2}{\mathbf{k}_i^2 \cos^2\theta_i} - 1\right]\epsilon_i, \tag{6}$$

where $\epsilon_i = \hbar^2 k_i^2 (2m)$ is the incident kinetic energy. This is called the scan curve equation.

Single-phonon excitations can be represented graphically by superimposing a scan curve [Eq. (6)] on top of a model form for the surface phonon dispersion curves. A single scan curve containing the data points from Fig. 4 is shown in an extended zone plot in Fig. 5; note that it intersects the dispersion curve in more than one place. Points 1 and 2 correspond to the Rayleigh mode (approximated by a sine curve). The two remaining points correspond to optical modes of higher phonon energy whose model dispersion relations are not shown. Finding a full dispersion curve requires a series

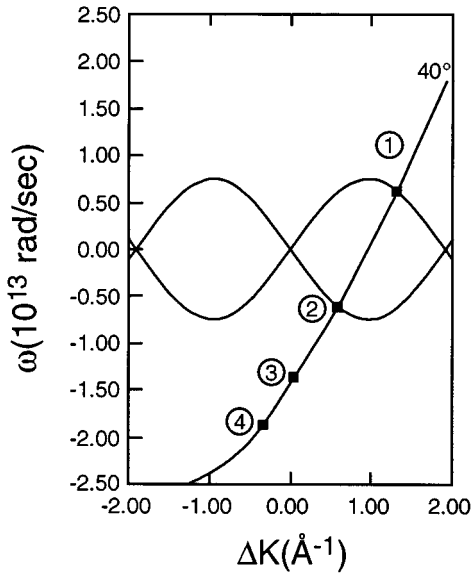

FIG. 5. The relation of a scan curve (solid line with numbers) for $k_i = 7.77$ Å^{-1}, $\theta_i = 40°$, compared to a surface phonon dispersion curve for a Rayleigh wave (approximated by a sine function) over an extended zone. The labeled points correspond to the peaks in Fig. 4 and those labeled 3 and 4 are from higher-energy optical modes.

of TOF measurements for different incident angles and sometimes different incident wave vectors.[8–10] Finally, the interpretation is greatly helped by comparison to lattice dynamical calculations, the topic of the next section.

In this work, an extensive set of TOF measurements for a fixed incoming wave vector $\mathbf{k}_i$, for a series of scattering angles and at 1-, 2-, and 3-ML coverages in the ⟨100⟩ and ⟨110⟩ directions have been performed to obtain experimental dispersion curves for each coverage. In Fig. 6, we show the experimental points for coverages of 1, 2, and 3 ML superimposed on calculated surface-phonon dispersion curves. Panels (a), (c), and (e) show all of the calculated modes, which include the shear vertical and longitudinal modes lying in the sagittal plane and the shear horizontal modes lying perpendicular to this plane. In panels (b), (d), and (f), projections of the z-polarized components are shown shaded to give a relative indication of the surface density of states. The calculations are discussed in the next section.

Note that there is both real and apparent scatter in the data, which can be attributed to several factors. First and probably the most important source for real scatter is that the positions of the phonon peaks in the TOF spectra were determined visually by locating a cursor at the peak where the computer then gave the location. As can be seen in Fig. 4, this method should be adequate for the peaks labeled 2, 3, and 4 where the uncertainty is typically about one quarter of the full width at half maximum, or 0.3 to 0.4 meV. However, for the peak labeled 1, the uncertainty in position could be as large as 0.8 meV. The data are a collection of both types of peaks with most being of the form of the peaks labeled 2, 3, and 4 of Fig. 4. The uncertainties in the data likely lie between these two limits. There also is apparent scatter as a result of the comparison to the theory and this will be discussed further in the next section.

IV. THEORY

A. Shell model

The theoretical approach used to describe this system is based on the shell model, which in addition to short-range

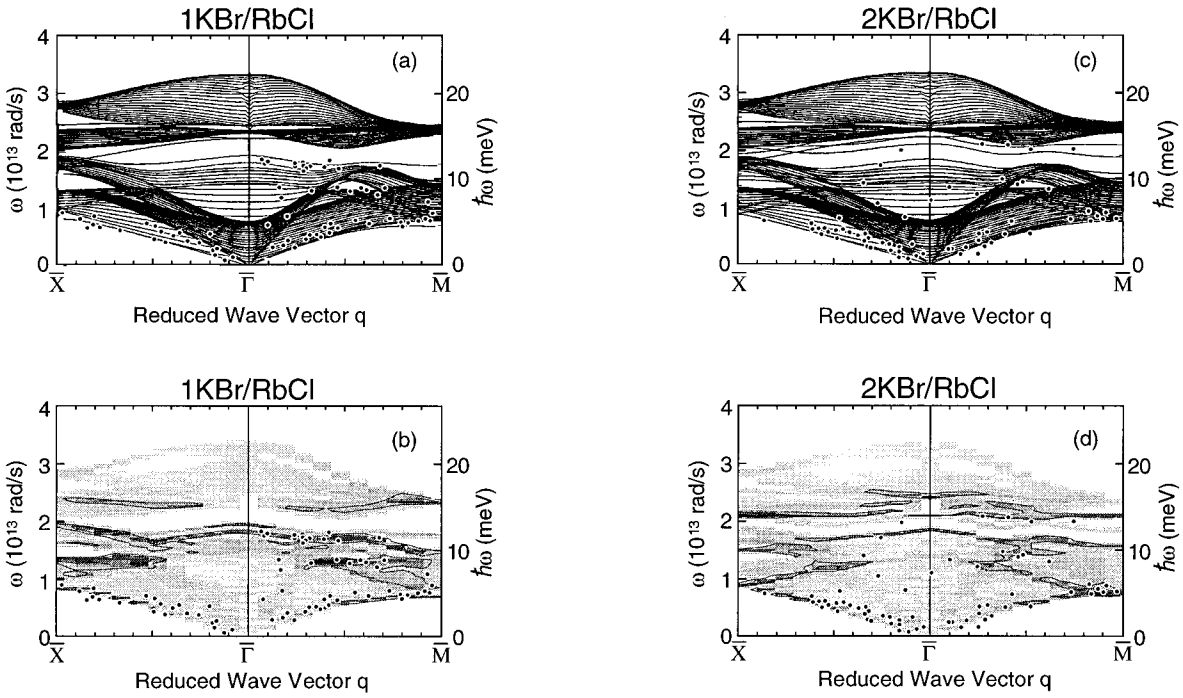

FIG. 6. The experimental data for the surface dispersion for coverages of 1, 2, and 3 ML of KBr on RbCl(001) superimposed on the slab calculations described in this work. (a), (c), and (e) contain the shear horizontal, the shear vertical and the longitudinal modes, while (b), (d), and (f) are plots of the z-projected density of the surface vibrations. The shading is an indication of the strength of the z-polarized density.

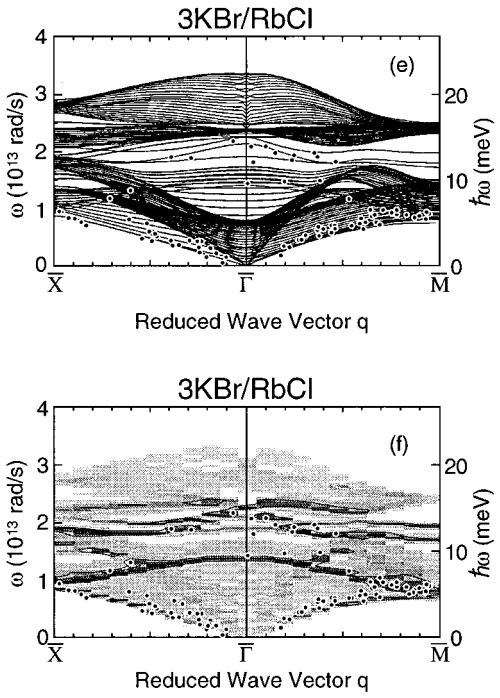

FIG. 6. (*Continued*).

and Coulomb interactions also takes the polarizability of the ions into account.[21,26] For the calculation of the surface relaxation and dynamics of clean alkali halide surfaces, good results are often obtained by simply using the model parameters found from a fit to measured bulk dispersion curves without modifications of force constants near the surface.[25] However, when the KBr/RbCl system is described within this framework several difficulties arise: (1) the Rb-K and Br-Cl interactions are not known from the bulk fits; (2) the commonly used shell models employ different ionic charges and polarizabilities for the same ions in different bulk materials; and (3) the Rb-Rb short-range interaction parameters used in these shell models of RbCl and RbBr are not consistent (the same holds for the K-K, Cl-Cl, and Br-Br interaction).

Following the work of Sangster *et al.*[19,20] we are able to obtain a consistent description of the bulk alkali halides RbCl, RbBr, KCl, and KBr, which uses one ionic charge for all crystals, one polarizability per ion, one shell charge per ion, and one set of Born-Mayer parameters for interactions between identical ions. To do this, we used the following form for the short-range potential acting between the shells of nearest-neighbor and next-nearest-neighbor atoms i and j:

$$V_{i,j}^{\mathrm{SR}}(r)=V_{i,j}^{\mathrm{vdW}}(r)+V_{i,j}^{\mathrm{BM}}(r), \tag{7}$$

with the Born-Mayer potential given by

$$V_{i,j}^{\mathrm{BM}}(r)=a_{i,j}\exp(-b_{i,j}r), \tag{8}$$

and the van der Waals interaction

$$V_{i,j}^{\mathrm{vdW}}(r)=\frac{c_{i,j}}{r^6}+\frac{d_{i,j}}{r^8}. \tag{9}$$

TABLE II. Potential parameters for the bulk materials.

	Rb	Cl	K	Br
Ionic charge (e)		0.9865		
$Y(e)$	7.60	−3.21	4.47	−3.11
d_i (Å^3)	0.33	−0.75	0.43	−1.19
α_i (Å^3)	2.50	2.41	1.92	3.69
	RbCl	KBr	RbBr	KCl
r_0 (Å)	3.259	3.262	3.410	3.116
A_{+-}	13.75	13.55	14.38	13.16
A_{++}	−0.13	−0.19	−0.09	−0.22
A_{--}	−0.23	−0.24	−0.38	−0.16
B_{+-}	−1.24	−1.35	−1.30	−1.29
B_{++}	0.01	0.03	0.01	0.03
B_{--}	0.04	0.08	0.07	0.04

The coefficients $c_{i,j}$ and $d_{i,j}$, calculated according to Ruffa,[22] depend only on the shell charges Y_i and the harmonic core-shell coupling constants k_i.

Using common notation, the longitudinal and transverse force constants of the Born-Mayer potential are

$$\frac{A_{i,j}^{\mathrm{BM}}}{2}\frac{e^2}{2r_0^3}=\left.\frac{\partial^2 V_{i,j}^{\mathrm{BM}}}{\partial r^2}\right|_{r=r_{i,j}}, \tag{10a}$$

$$\frac{B_{i,j}^{\mathrm{BM}}}{2}\frac{e^2}{2r_0^3}=\frac{1}{r}\left.\frac{\partial V_{i,j}^{\mathrm{BM}}}{\partial r}\right|_{r=r_{i,j}}, \tag{10b}$$

and similarly for the van der Waals interaction. Here r_0 is the distance between nearest neighbors and $r_{i,j}$ is the equilibrium distance between atoms i and j in the bulk. The total short-range force constants are then the sum of the Born-Mayer and the van der Waals contributions

$$A_{i,j}=A_{i,j}^{\mathrm{BM}}+A_{i,j}^{\mathrm{vdW}}, \quad B_{i,j}=B_{i,j}^{\mathrm{BM}}+B_{i,j}^{\mathrm{vdW}}. \tag{11}$$

These model parameters are fitted to the following bulk properties: (1) Dielectric properties, i.e., static dielectric constant, high-frequency dielectric constant. (2) Elastic constants C_{11} and C_{12}. Since our model fulfills the equilibrium condition we obtain the Cauchy relation $C_{12}=C_{44}$. (3) Phonon frequencies at the Γ, X, and L points obtained from neutron scattering. (4) Cohesive energy of the bulk. (5) Pressure derivative of C_{44}. Note that (4) and (5) provide information about the interatomic forces, which is not included in (1)–(3). The potential parameters of the four bulk materials are given in Table II.

At this point a description for the Rb-K and the Cl-Br interaction is still missing. However, since the nature of the Rb-K is expected to be similar to the Rb-Rb and the K-K interactions, we apply the following form for these force constants:

$$A_{\text{Rb-K}}^{\mathrm{BM}}=\tfrac{1}{2}(A_{\text{Rb-Rb}}^{\mathrm{BM}}+A_{\text{K-K}}^{\mathrm{BM}}), \ldots . \tag{12}$$

TABLE III. Comparison between experimental data and model value. The theoretical value is written above the experimental value. Experimental data were all taken from Refs. 19, 20, and 23 except the frequencies for KCl at the X point, which were taken from Copley, Macpherson, and Timusk (Ref. 24). The values given by Copley, Macpherson, and Timusk allowed for a more consistent fit with other data.

	RbCl	KBr	RbBr	KCl
Cohesive energy (eV)	1.11	1.10	1.07	1.15
	1.11	1.10	1.06	1.15
α_0/V (Å^3)	0.129	0.131	0.127	0.129
	0.129	0.130	0.129	0.128
α_∞/V (Å^3)	0.068	0.075	0.074	0.068
	0.068	0.076	0.075	0.068
F_0 (Å^3)	0.156	0.146	0.140	0.166
	0.159	0.146	0.142	0.168
C_{11} (10^{11} dyn cm^2)	4.33	4.21	3.85	4.82
	4.30	4.21	3.86	4.83
$\frac{1}{2}(C_{12}+C_{44})$ (10^{11} dyn cm^2)	0.59	0.56	0.46	0.69
	0.57	0.54	0.44	0.66
$\partial C_{44}/\partial p$	−0.63	−0.33	−0.61	−0.40
	−0.56	−0.33	−0.55	−0.40
$\omega_{\mathrm{LO}}(X)$ (10^{13} rad/s)	2.48	2.49	1.86	2.99
	2.52	2.53	1.86	2.95
$\omega_{\mathrm{LA}}(X)$ (10^{13} rad/s)	1.45	1.35	1.11	2.00
	1.43	1.35	1.12	2.03
$\omega_{\mathrm{TO}}(X)$ (10^{13} rad/s)	2.39	2.35	1.82	2.90
	2.39	2.33	1.80	2.85
$\omega_{\mathrm{TA}}(X)$ (10^{13} rad/s)	0.79	0.76	0.60	1.07
	0.82	0.79	0.62	1.11
$\omega_{\mathrm{LO}}(L)$ (10^{13} rad/s)	2.86	2.78	1.84	3.00
	2.77	2.73	1.82	2.98
$\omega_{\mathrm{LA}}(L)$ (10^{13} rad/s)	1.92	1.81	1.73	2.92
	1.92	1.77	1.74	2.92
$\omega_{\mathrm{TO}}(L)$ (10^{13} rad/s)	2.08	1.92	1.34	2.14
	2.13	1.93	1.32	2.17
$\omega_{\mathrm{TA}}(L)$ (10^{13} rad/s)	1.33	1.37	1.28	2.02
	1.29	1.38	1.31	2.01

This provides us with a complete description of the layered system within the shell model. Additional details on comparison of experimental and calculated parameters are given in Table III.

B. Relaxation and slab dynamics

The surface relaxation is determined with a Newton-Raphson technique described by de Wette, Kress, and Schröder.[34] As in the case of clean alkali halide surfaces, the magnitude of the relaxation decreases rapidly going into the surface and the maximum displacements are the same as the lattice constants to within a few percent. We observe a rumpling of the core positions of the RbCl interface layer of 0.07 Å due to an outwards motion of the negative ion, which is almost independent of the number of adlayers.

The curves in Figs. 6(a)–6(f) show the calculated slab dynamics including relaxation for 1, 2, and 3 ML of KBr. The slab dynamics formalism is that described in Kress *et al.*[35] The total width of the slab corresponds to 25 layers. Note that the three lower panels show the z-polarized components of the top layer of the calculated dispersion curves.

The data likely contain some longitudinal modes at low energies near the surface Brillouin zone center. These are not projected out by the theory in the lower panels and will appear as ''apparent'' scatter in the data, which adds to the comment on uncertainty made in the previous section. In addition there is width in the density of phonon states at the surface that could give peaks with ''apparent'' scatter as in Fig. 6.

Additionally, we show in Figs. 7(a)–7(d) the surface dynamical results for the KBr, KCl, RbCl, and RbBr, with these theoretical results obtained from the same potential parameters as used for the growth work.[9,36–38]

V. DISCUSSION

Upon close examination of the data for the 1-, 2-, and 3-ML cases, it can be seen that the Rayleigh modes look similar for all three cases. It is in the z-projected optical mode (and particularly for the $\overline{\Gamma M}$ direction) where experimental results differ from layer to layer. Note that the 1-ML case looks very different from that of clean RbCl.[37] This was already in evidence in the angular distribution for the 1-ML KBr/RbCl case (not shown) where the shift to the corrugation of KBr had already started and was clearly in evidence in the angular distribution of Fig. 3 for the 2-ML case.

The z-projected optical mode in the $\overline{\Gamma M}$ direction first increases in energy in going from 1 ML to 2 ML and decreases again at 3 ML. This behavior is fit well by the calculated results. In addition, the 3-ML case agrees quite well with the clean KBr surface dynamical results as in Fig. 7.[9] Although the latter has more experimental data, the evidence is reasonably clear in comparison and suggests that by 3 ML, the grown KBr surface has nearly the same surface dynamics as that of a surface measured from a bulk KBr sample.

In Fig. 8, we break out the optical mode region so that the comparison for clean RbCl, the three layered cases, and clean KBr can be made visually. Note the shift in optical mode with coverage and the good agreement between the data and the theory. It is this region of the data that puts the most stringent requirements on the theory used to obtain the fit.

Using the same potential parameters, the fits to the surface dispersion of KBr, KCl, RbCl, and RbBr are all very acceptable, and since the original parameters used in the calculations were from bulk dispersion data, the bulk curves are also in agreement with these parameters.[9,36–38] The bulk fits are not included in this work. We comment that the new parameters provide a theoretical fit for the RbBr surface dispersion measurements, which agrees better than the one used previously where relaxation was predicted to produce an optical mode in the dispersion curve that was shifted upward in energy.[38] This was not observed experimentally and at that time the reason for it was not clear. This work provides the answer, predicting a smaller relaxation than what was previously calculated, which does not lead to the higher-energy surface-phonon mode.

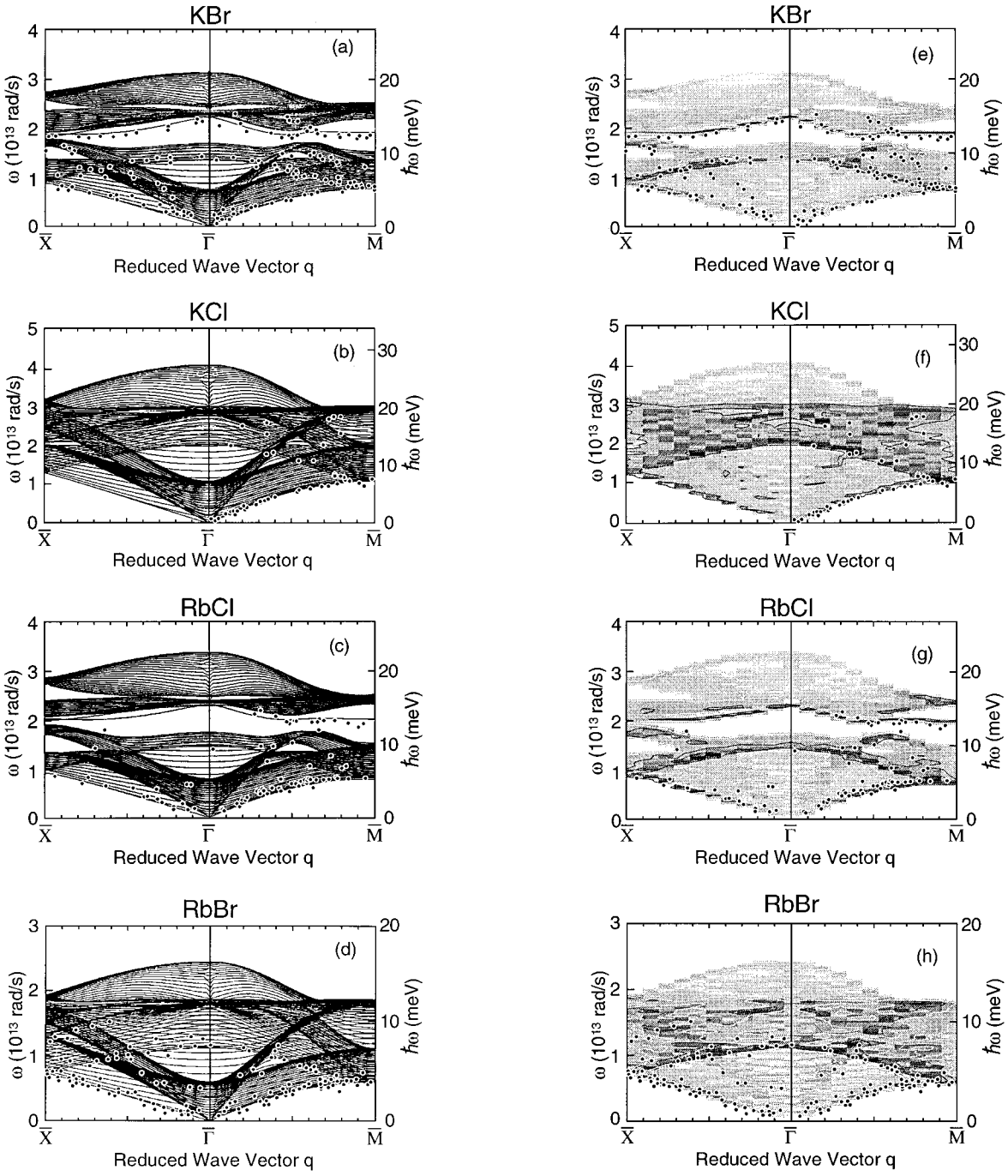

FIG. 7. The experimental data for the surface dispersion for the clean surfaces of KBr, KCl, RbCl, and RbBr compared to the calculated dynamics, which were obtained using the same potential parameters as used for the calculations of the previous figure. (a)–(d) show all of the modes, while (e)–(h) are the z-projected density of the surface vibrations for the respective surface.

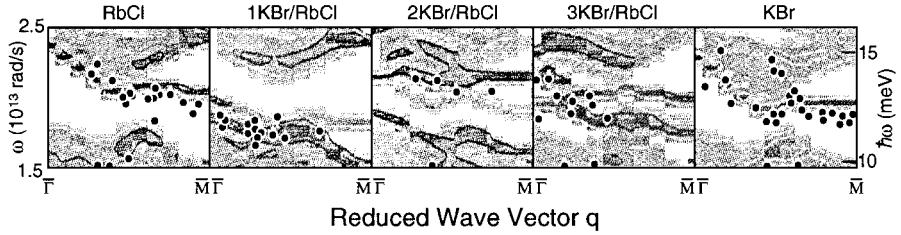

FIG. 8. A comparison of the experimental data and the theory for the optical mode region for clean RbCl, the three grown layers and clean KRb. It is this mode that changes the most and puts the greatest demands on the comparison of the data to the theory. Note the good comparison of the experiment and theory.

VI. CONCLUSIONS

The results of this work impose the same shell-model parameters on a wide range of data. The theoretical modeling used in the slab calculations provides close agreement with the measured dispersion curves for coverages of 1-, 2-, and 3-ML coverages of KBr on RbCl(001) as well for the clean surfaces of KBr, KCl, RbCl, and RbBr. Further, the modeling is in agreement with the bulk dynamics, which when taken all together represents an extensive range of data.

This forces additional constraints on the shell models that can be used.[14] For example, the $\partial C_{44}/\partial p$ term in Table III is ill conditioned by bulk shell-model fits. However, in this work, where relaxation takes place, the term is important.

These results encourage us to suggest that much of the growth of ionic materials might be interpreted in a similar fashion and that these same methods might carry forward to the metal oxides such as NiO, CoO, and MgO as well as other materials that also can be treated by shell-model methods.

The present work has looked only at the surface dispersion relations. There is more information available if the shape of the scattered time-of-flight peaks can be measured as well as their position. At present the instrument does not have adequate signal-to-noise capability, however, these improvements are planned and, thus, a next step would be to measure the spectra very carefully with improved signal-to-noise and longer measuring times to determine the uniqueness of the model by trying to fit the shape of the spectra as well as the dispersion curves. This should provide for a comparison to surface-phonon density of states and impose additional conditions on the shell model parameters.

ACKNOWLEDGMENTS

This research was supported by DOE Grant No. DE-FG05-85ER45208 and NATO Grant No. 891059. Computer support was provided by the Supercomputer Computations Research Institute (SCRI). One of the authors (E.S.G.) acknowledges the support of the Hitachi Advanced Research Laboratory while preparing this manuscript. Partial support for this work came from the Deutsche Forschungsgemeinschaft through the Graduierten Kolleg ''Komplexität in Festkörpen: Phonon, Elektronen, und Strukturen.''

*Present address: Advanced Research Laboratory, Hitachi, Ltd., Hatoyama, Saitama 350-03, Japan.

[1] M. A. Herman and H. Sitter, *Molecular Beam Epitaxy*, Springer Series in Materials Science Vol. 7 (Springer-Verlag, Berlin, 1989).
[2] *Molecular Beam Epitaxy* (Ref. 1), Chap. 4.
[3] J. M. Van Hove, P. R. Pukite, and P. I. Cohen, J. Vac. Sci. Technol. B **3**, 563 (1985).
[4] M. H. Yang and C. P. Flynn, Phys. Rev. Lett. **62**, 2467 (1989).
[5] M. H. Yang and C. P. Flynn, Phys. Rev. B **41**, 8500 (1990).
[6] K. S. Song and R. T. Williams, *Self-Trapped Excitons* (Springer-Verlag, Berlin, 1993).
[7] W. F. Egelhoff and I. Jacob, Phys. Rev. Lett. **62**, 921 (1989).
[8] G. Brusdeylins, R. B. Doak, and J. P. Toennies, Phys. Rev. B **27**, 3662 (1983).
[9] G. Chern, J. G. Skofronick, W. P. Brug, and S. A. Safron, Phys. Rev. B **39**, 12 828 (1989).
[10] J. P. Toennies, in *Surface Physics*, edited by W. Kress (Springer-Verlag, Berlin, 1991), Chap. 5.
[11] J. J. de Miguel, A. Cebollada, J. M. Gallego, J. Ferrón, and S. Ferrer, J. Cryst. Growth **88**, 442 (1988).
[12] K. D. Gibson and S. J. Sibener, Phys. Rev. Lett. **55**, 514 (1985); Farad. Discuss. Chem. Soc. **80**, 203 (1985).
[13] K. D. Gibson and S. J. Sibener, J. Chem. Phys. **88**, 7862 (1988).
[14] H. Bilz and W. Kress, *Phonon Dispersion Relations in Insulators* (Springer-Verlag, Berlin, 1979).
[15] W. Kress and F. W. deWette, *Surface Phonons*, Springer Series in Surface Science Vol. 21 (Springer-Verlag, Berlin, 1991).
[16] J. Juan, G. G. Bishop, E. S. Gillman, G. Chern, S. A. Safron, and J. G. Skofronick, J. Vac. Sci. Technol. A **10**, 1999 (1992).
[17] S. A. Safron, J. Duan, G. G. Bishop, E. S. Gillman, and J. G. Skofronick, J. Phys. Chem. **97**, 1749 (1993).
[18] J. G. Skofronick, G. G. Bishop, J. Duan, E. S. Gillman, S. A. Safron, D. Bonart, and U. Schröder, J. Electron. Spectrosc. Relat. Phenom. **64/65**, 747 (1993).
[19] M. J. Sangster, U. Schröder, and R. M. Atwood, J. Phys. C **11**, 1523 (1978).
[20] M. J. Sangster and R. M. Atwood, J. Phys. C **11**, 1541 (1978).
[21] R. A. Cowley and W. Cochran, Phys. Rev. **131**, 1030 (1963).
[22] A. R. Ruffa, Phys. Rev. **130**, 1412 (1963).
[23] V. K. Garg, D. S. Puri, and M. P. Verma, Phys. Status Solidi B **80**, 63 (1977).
[24] J. R. D. Copley, R. W. Macpherson, and T. Timusk, Phys. Rev. **182**, 965 (1969).
[25] T. S. Chen, F. W. de Wette, and G. P. Alldredge, Phys. Rev. B **15**, 1167 (1977).
[26] B. G. Dick and A. W. Overhauser, Phys. Rev. **112**, 90 (1962).
[27] R. B. Doak, in *Atomic and Molecular Beam Methods*, edited by G. Scoles (Oxford University Press, New York, 1992), Vol. 2, p. 384.
[28] R. David, K. Kern, P. Zeppenfeld, and G. Comsa, Rev. Sci. Instrum. **57**, 2771 (1986).
[29] Utah Crystal Growth Laboratory, University of Utah, Physics Department, Salt Lake City, UT 84112.
[30] J. Duan, Ph. D. dissertation, Florida State University, 1992.
[31] S. A. Safron, G. G. Bishop, J. Duan, E. S. Gillman, J. G. Skofronick, N. S. Luo, and P. Ruggerone, J. Phys. Chem. **97**, 2270 (1992).
[32] J. Duan, G. G. Bishop, E. S. Gillman, G. Chern, S. A. Safron, and J. G. Skofronick, Surf. Sci. **272**, 220 (1992).
[33] J. R. Manson, Phys. Rev. B **43**, 6924 (1991).
[34] F. W. deWette, W. Kress, and U. Schröder, Phys. Rev. B **32**, 4143 (1985).
[35] W. Kress, F. W. deWette, A. D. Kulkarni, and U. Schröder, Phys. Rev. B **35**, 5733 (1987).
[36] G. Benedek, G. Brusdeylins, R. B. Doak, and J. P. Toennies, J. Phys. (Paris) Colloq. Suppl. 12, **42**, C6-793 (1981).
[37] G. G. Bishop, J. Duan, E. S. Gillman, S. A. Safron, and J. G. Skofronick, J. Vac. Sci. Technol. A **11**, 2008 (1993).
[38] G. Chern, J. G. Skofronick, W. P. Brug, and S. A. Safron, Phys. Rev. B **39**, 12 838 (1989).